JACS
JOURNAL OF THE AMERICAN CHEMICAL SOCIETY
pubs.acs.org/JACS
Article

Type-I CdS/ZnS Core/Shell Quantum Dot-Gold Heterostructural Nanocrystals for Enhanced Photocatalytic Hydrogen Generation

Na Jin, Yonglei Sun, Wenwu Shi, Ping Wang, Yasutaka Nagaoka, Tong Cai, Rongzhen Wu, Lacie Dube, Hawi N. Nyiera, Yuzi Liu, Tomoyasu Mani, Xinzhong Wang, Jing Zhao, and Ou Chen*

Cite This: J. Am. Chem. Soc. 2023, 145, 21886−21896

ABSTRACT: Developing Type-I core/shell quantum dots is of great importance toward fabricating stable and sustainable photocatalysts. However, the application of Type-I systems has been limited due to the strongly confined photogenerated charges by the energy barrier originating from the wide-bandgap shell material. In this project, we found that through the decoration of Au satellite-type domains on the surface of Type-I CdS/ZnS core/shell quantum dots, such an energy barrier can be effectively overcome and an over 400-fold enhancement of photocatalytic H_2 evolution rate was achieved compared to bare CdS/ZnS quantum dots. Transient absorption spectroscopic studies indicated that the charges can be effectively extracted and subsequently transferred to surrounding molecular substrates in a subpicosecond time scale in such hybrid nanocrystals. Based on density functional theory calculations, the ultrafast charge separation rates were ascribed to the formation of intermediate Au_2S layer at the semiconductor−metal interface, which can successfully offset the energy confinement introduced by the ZnS shell. Our findings not only provide insightful understandings on charge carrier dynamics in semiconductor−metal heterostructural materials but also pave the way for the future design of quantum dot-based hybrid photocatalytic systems.

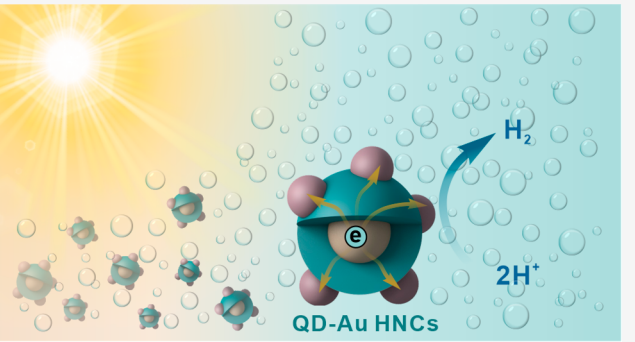

1. INTRODUCTION

Over the past few centuries, rapid industrialization has led to a myriad of issues, such as environmental pollution and energy shortages, necessitating the need for exploring sustainable energy sources that are both produced in an environmentally friendly manner and consumed without further releasing contaminants.[1−3] In this regard, solar-driven photocatalytic hydrogen (H_2) evolution reaction (HER) has been extensively studied in both academia and industry and is considered as a strong contender for partially replacing fossil fuels.[4,5] Since the pioneering work reported by Fujishima and Honda for electrochemical photolysis of water using TiO_2,[6] the structures and photocatalytic performances of all kinds of inorganic semiconductor-based photocatalysts have been extensively researched.[7,8] Among them, CdS stands out due to its appropriate bandgap (2.4 eV) and band offset,[9] enabling absorption of the visible spectrum while maintaining relatively strong redox abilities.[10] Especially, when downsizing CdS semiconductor material to a few nanometers (nm), CdS nanocrystals (NCs), also known as quantum dots (QDs), offer additional advantages as photocatalysts, including tunable optical and electronic profiles,[11] improved atom utilization efficiency,[12] and solution dispersibility and processability.[13] Despite these advantages, CdS QDs are susceptible to deterioration under photoirradiation, especially in oxygen-containing aqueous solutions.[14] Such photocorrosion leads to the degradation of the catalysts' overall integrity, resulting in decreased catalytic efficiency and the release of the toxic Cd element.[15] In addition, deep trap states on the CdS QDs' surface serve as sites for fast exciton (i.e., electron and hole pair) recombination,[16] significantly reducing the number of available photogenerated charge carriers for catalysis. These constraints have largely limited the application of CdS QDs as reliable catalysts in various reactions, including photocatalytic H_2 production.[17] To avoid the decomposition of CdS QDs and passivate their surface states, one important strategy is to grow a "shell" of another semiconductor material to produce core/shell structured QDs and physically isolate the active "core" QDs from the surrounding environment.[18−20] In this context, the ZnS semiconductor has been identified as a suitable eco-friendly shell material that can provide protection for the CdS core QDs from photo- and/or physical-degradations while preserving their optical absorption or redox potentials.[21]

Received: June 9, 2023
Published: September 28, 2023

https://doi.org/10.1021/jacs.3c06065
J. Am. Chem. Soc. 2023, 145, 21886−21896

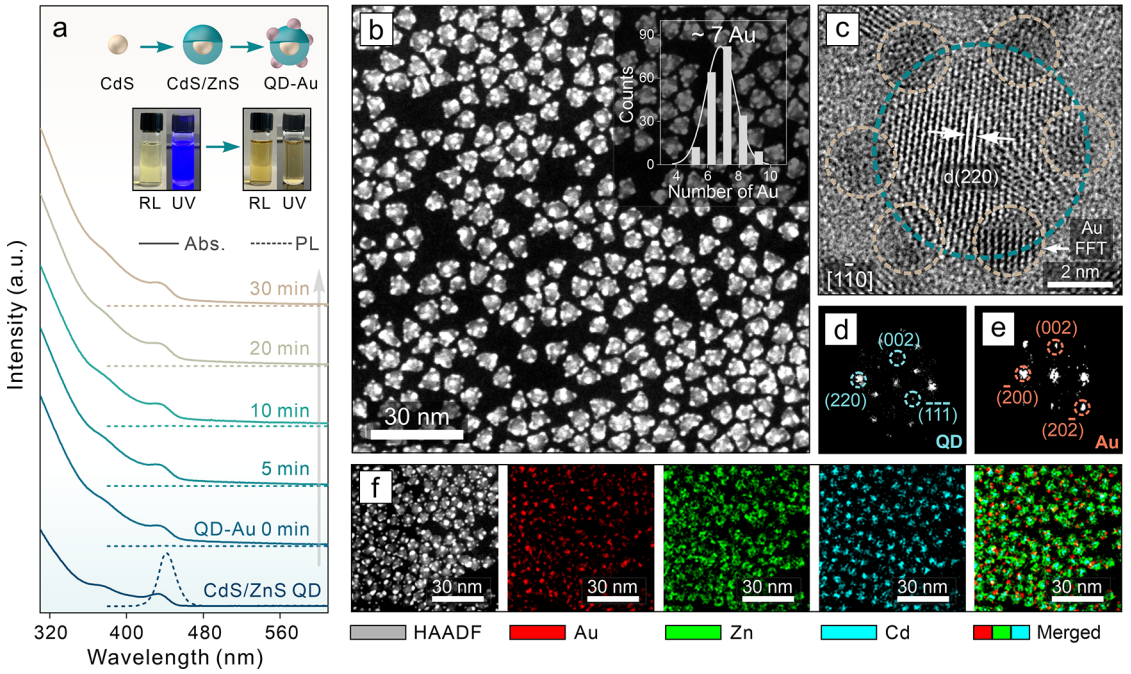

Figure 1. Characterizations of QD-Au HNCs. (a) Absorption and PL spectral evolution during Au growth. Insets: synthetic steps (top) and photographs (bottom) of QDs (bottom left) and QD-Au HNCs (bottom right) under room light (RL) and ultraviolet (UV) light illumination. (b) A HAADF-STEM image of QD-Au HNCs. Inset: histogram of the number of Au domains per QD. (c) HR-TEM image of a QD-Au HNC; and (d, e) the corresponding FFT patterns of the QD (d) and Au (e) domains. (f) Elemental mapping of QD-Au HNCs showing the distribution of Au, Zn, and Cd elements.

However, the resulting CdS/ZnS core/shell QDs possess a so-called Type-I band alignment (i.e., the bandgap of the core is embedded in the wider bandgap of the shell),[18] in which both electrons and holes are strongly confined in the semiconductor core region (i.e., CdS core QDs). The low availability of the charge carriers has therefore limited the practical applications of Type-I core/shell QDs in photocatalytic reactions.[22−25] In the meantime, semiconductor−metal heterostructural nanocrystals (HNCs) that couple semiconductor NCs with metal NCs have emerged as unique photocatalysts for fuel production with significantly improved efficiency.[26−32] Research efforts have been devoted to the delicate synthetic control of HNCs with diverse compositions and morphologies,[33,34] which also allow for the study of novel properties generated from the nanoscale semiconductor−metal heterojunction, such as ultrafast charge transfer.[35−41] Regardless of the thorough investigations in the morphology control and synergistic effects, the synthesis and utilization of semiconductor−metal HNCs containing Type-I core/shell QDs for photocatalytic reactions have not yet been clearly demonstrated.

Herein, we showed that by decorating metallic Au crystalline domains on the CdS/ZnS core/shell QDs, the inert Type-I system can be catalytically activated. We synthesized CdS/ZnS QD-Au host-satellite-type HNCs with multiple metallic Au domains randomly distributed on the QD host surface. By varying the ratio of Au precursors to QDs, the diameter of the Au domains can be tuned from 1.6 to 3.3 nm. The catalytic performance of the QD-Au HNCs showed a negative dependence on the size of the Au domains, and a maximum of over four-hundred-fold enhancement of HER rate can be reached comparing to the bare CdS/ZnS QDs counterpart. Transient absorption (TA) spectroscopic results indicated that the deposition of Au domains on CdS/ZnS QDs can enhance the catalytic efficiency through facilitating the electron extraction to the Au domains and further transfer to electron accepting molecules. Density functional theory (DFT) calculations demonstrated that such an ultrafast charge separation was partly due to the formation of the Au_2S layer at the semiconductor−metal interface, which can relax the energy barrier installed by the ZnS shell material, thus increasing the surface electron population of HNCs for subsequent hydrogen generation through proton reduction. Overall, we demonstrated that the decoration of small Au domains onto CdS/ZnS QDs served as an effective approach to activate Type-I systems for photocatalytic HER, which will provide insights into the design and discovery of next-generation heterostructure-based artificial photocatalysts.

2. RESULTS AND DISCUSSION

2.1. Synthesis and Characterization of CdS/ZnS QD-Au Host-Satellite HNCs. The CdS/ZnS core/shell QD-Au HNCs were synthesized following a three-step procedure (experimental details can be found in the Supporting Information (SI)),[42] and aliquots were taken to monitor the reaction. First, CdS core QDs were prepared by a heating-up approach,[43] and the resulting CdS cores possessed a first excitonic peak centered at 435 nm (Figure S1). Next, four monolayers (MLs) of ZnS shell were grown onto the CdS core QDs using a successive ionic layer adsorption and reaction method;[44,45] and the UV−vis absorption spectra, photoluminescence (PL) spectra, and transmission electron microscopic (TEM) images after growth of each ML of ZnS shell were presented in Figures S1−S3. The increase in absorption in the UV region as well as the gradual quenching of CdS surface trap emission demonstrated successful ZnS shell growth. The excitonic absorption peak position showed nearly no shift before and after ZnS shell formation, indicating the

https://doi.org/10.1021/jacs.3c06065
J. Am. Chem. Soc. 2023, 145, 21886−21896

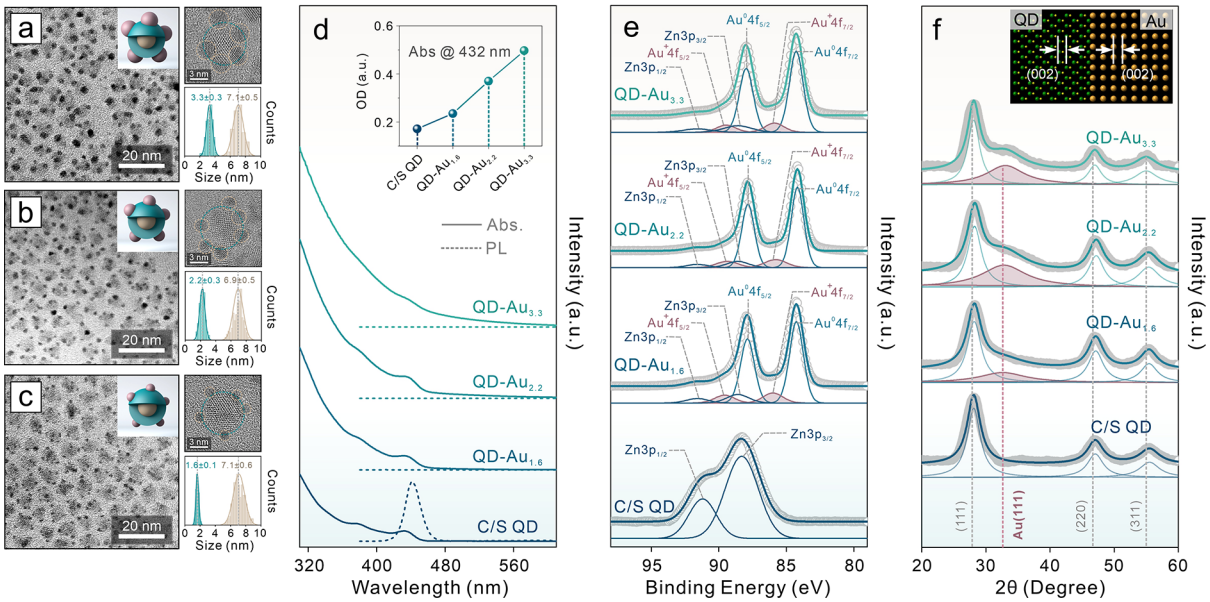

Figure 2. Characterizations of QD-Au HNCs with different Au satellite domain sizes. (a–c) TEM images (left), HR-TEM images (top right), and size distribution histograms (bottom right) of QD-$Au_{3.3}$ (a), QD-$Au_{2.2}$ (b), and QD-$Au_{1.6}$ (c) HNCs. (d) Absorption and PL spectra of CdS/ZnS core/shell (C/S) QDs, and three QD-Au HNC samples with different Au domain sizes. Inset: Optical density (OD) at the first excitonic peak of HNCs with increasing Au domain sizes. (e, f) XPS spectra and XRD patterns of the QD and three QD-Au HNC samples. Inset of (f): Atomic model showing the interface between the QD host and the Au satellite domain.

Type-I core/shell band alignment with a strong quantum confinement.[46] The average PL lifetime of the final CdS/ZnS core/shell QDs was determined to be 30.8 ns through a three-component exponential tail fitting (Figure S4 and Table S1). TEM images suggested good dispersibility and a narrow size distribution of the synthesized core/shell QDs (Figure S5). The average size of the QDs was 7.1 ± 0.6 nm, which agreed well with the calculated particle size based on the thickness of each ZnS shell atomic layer (0.31 nm).[47] The deposition of Au satellite domains onto the QD host surface was then achieved by thermally reducing $AuCl_3$ using oleylamine as a weak reducing agent (see details in SI).[48] Figure 1a presented the absorption and PL spectral evolutions during the Au growth stage with a constant QD concentration of 0.25 nmol/mL. Quantitative analysis demonstrated an increased optical density at the first excitonic peak (at 432 nm) of the QD host owing to the contribution of Au absorption, which was a featureless broad absorption tail extending from the UV to the visible spectral range,[49,50] confirming the Au satellite domain formation (Figure S6). Meanwhile, the PL of QDs was totally quenched immediately after the Au precursor injection (Figure 1a, Figure S6), indicating that the Au deposition efficiently prevented the excitonic radiative recombination in the QD host.[51] The morphology of QD-Au HNCs and the distribution of Au domains on the QD surface were demonstrated in Figure 1b–f. As shown in high-angle annular dark field scanning TEM image (HAADF-STEM, Figure 1b), around 7 Au domains in average were randomly distributed on each QD host, following a Volmer–Weber growth model.[34] High-resolution TEM (HR-TEM, Figure 1c) images exhibited clear lattice fringes for both QD hosts and Au satellite domains, suggesting a high crystallinity of the HNCs. Analyses based on the *d*-spacings and the corresponding fast-Fourier transformation (FFT) patterns revealed that the Au domains grew onto the QD host surface through sharing the common (002) crystal plane (Figure 1d, e), in line with our previous studies on a similar HNC system.[28] Elemental mapping results served as additional evidence for the heterostructure of the CdS/ZnS QD-Au HNCs that comprised core/shell QDs and Au domains on the surface (Figure 1f).

2.2. Synthesis of QD-Au HNCs with Different Au Domain Sizes. Next, we synthesized three QD-Au HNC samples with different Au domain sizes by adjusting the feeding ratio of $AuCl_3$ precursors to QDs (see SI for synthetic details). The average Au domain sizes of 1.6 ± 0.1 nm (QD-$Au_{1.6}$), 2.2 ± 0.3 nm (QD-$Au_{2.2}$), and 3.3 ± 0.3 nm (QD-$Au_{3.3}$) were achieved without alteration of the QD host diameter (Figure 2a–c). Energy-dispersive X-ray spectroscopic (EDS) measurements revealed an increased Au atomic ratio, parallel to the increased size of Au domains as shown in the TEM measurements (Table S2, Figure S7–10). Figure 2d presented the absorption and PL spectra of CdS/ZnS core/shell QDs and three QD-Au HNC samples. While no PL was observed for all of the HNC samples, an increased optical density at the QD first absorption peak can be observed when increasing the Au domain size (Figure 2d). X-ray photoelectron spectroscopic (XPS) measurements clearly showed two major characteristic peaks of Au^0 centered at around 84.2 eV ($4f_{7/2}$) and 87.9 eV ($4f_{5/2}$) for all three HNC samples (Figure 2e).[52] Zn 3p peaks centered at around 88.5 eV ($3p_{3/2}$) and 91.5 eV ($3p_{1/2}$) were consistently observed in the CdS/ZnS QDs and three QD-Au HNC samples.[53] Interestingly, additional XPS features at around 85.9 and 89.5 eV can also be deconvoluted for the three QD-Au HNC samples, which were assigned to the Au^+ $4f_{7/2}$ and $4f_{5/2}$ peaks, respectively.[54] The presence of Au^+ signals indicated the formation of a Au_2S layer at the interface of ZnS shell and Au satellite domains, in agreement with previous observations for similar semiconductor–metal hybrid materials.[55,56] X-ray powder diffraction (XRD) patterns showed that the zinc-blende crystal structure of the CdS/ZnS QD hosts retained after the Au domain growth (Figure 2f).[44] An additional broad Bragg

https://doi.org/10.1021/jacs.3c06065
J. Am. Chem. Soc. 2023, 145, 21886–21896

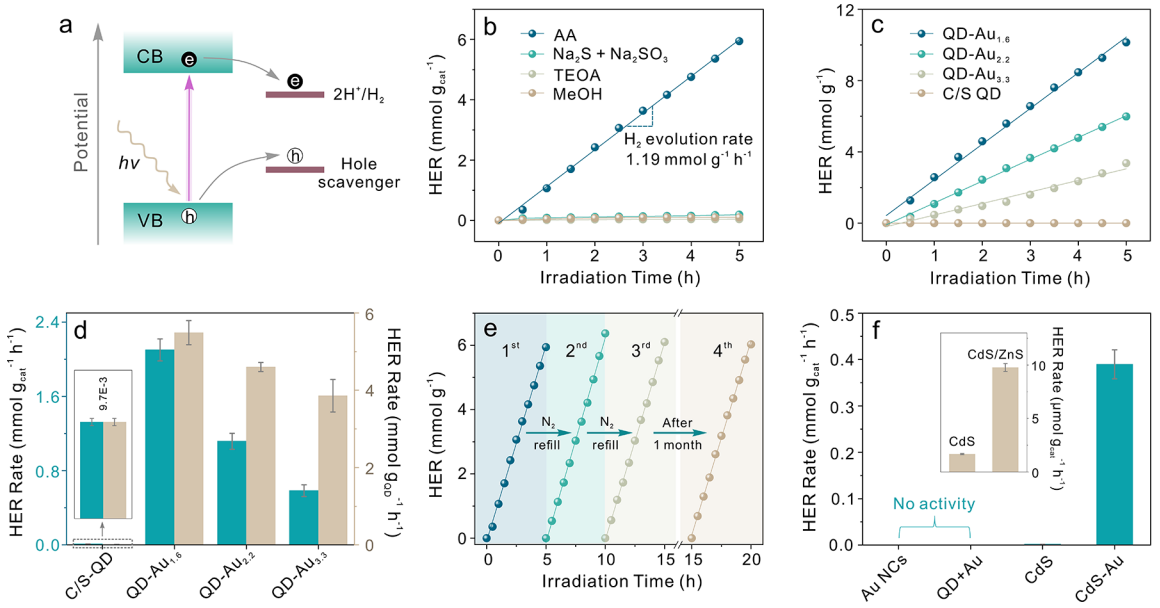

Figure 3. Catalytic performance characterizations of the QD-Au HNCs. (a) Scheme of the photoinduced excitonic and catalytic processes. (b) HER activity as a function of reaction time for QD-$Au_{2.2}$ HNCs with different hole scavengers. (c) HER activity as a function of reaction time for C/S QDs and three QD-Au HNC samples with different Au domain sizes. (d) HER rates of C/S QDs and three QD-Au HNC samples before and after normalization with mass of QDs. Inset: amplified HER rate of the C/S QD samples. (e) Cycling HER activities of the QD-$Au_{2.2}$ HNCs. (f) HER rates of the control groups using different photocatalysts: Au NCs, a mixture of C/S QDs and Au NCs (QD+Au), CdS QDs, and CdS-Au HNCs. Inset: HER rate comparison between CdS QDs and CdS/ZnS C/S QDs.

diffraction peak at 2θ of around 32.6°−33.0° was observed for all three QD-Au HNC samples, which can be assigned to the (111) crystal plane of the Au crystalline domains.[28,57] Only one clear diffraction peak of Au domains (i.e., Au(111)) can be resolved due to their small sizes.[58] The calculated *d*-spacings of 2.74 Å (QD-$Au_{1.6}$), 2.73 Å (QD-$Au_{2.2}$), and 2.71 Å (QD-$Au_{3.3}$) suggested noticeable Au lattice expansions of 16.1%, 15.7%, and 14.8% for the (111) crystal plane, respectively (Tables S3−S6), as a result of the large lattice mismatch between QD host materials (CdS: a_{CdS} = 5.88 Å; ZnS: a_{ZnS} = 5.41 Å) and Au domain lattices (Au: a_{Au} = 4.08 Å).[47,59,60]

2.3. Photocatalytic H_2 Evolution Performance of QD-Au HNCs. The complete quenching of the electron−hole radiative recombination of the Type-I CdS/ZnS core/shell QDs by Au growth drove us to explore the catalytic performance of QD-Au HNCs toward HER through photocatalytic proton reduction. Phase transfer was employed to render the obtained HNCs water-soluble. In this context, 11-mercaptoundecanoic acid (MUA) was utilized to transfer the relevant samples from toluene into water with close-to-unity transfer yield and nearly unchanged heterostructural morphology and optical properties (Figures S11−13). The successful ligand exchanges using MUA with a ligand weight ratio of ∼10% were characterized by nuclear magnetic resonance spectroscopy and thermogravimetric analysis (Figures S14, 15). We found that the MUA-capped QD-Au HNCs were stable in water for at least 10 months (Figure S16). The photocatalytic experiments were performed in an optical enclosure with 400 nm light irradiation (details of the experiments can be found in the SI). Hole scavengers were applied to avoid accumulation of holes within the HNC catalysts. A scheme of the photocatalytic process was shown in Figure 3a. First, we evaluated the efficiency of H_2 evolution with four commonly used hole scavengers, including ascorbic acid (AA), sodium sulfide and sodium sulfite (Na_2S + Na_2SO_3), triethanolamine (TEOA), and methanol (MeOH). As shown in Figure 3b, the catalytic reaction (using the QD-$Au_{2.2}$ HNCs as the catalysts) with AA as the hole scavenger showed a drastically higher H_2 evolution efficiency in comparison to that using the other three hole scavengers (Figure S17). A constant H_2 evolution rate of 1.19 mmol g_{cat}^{-1} h^{-1} for at least 5 h was observed (Figure 3b). The large difference of the catalytic reactivity with different hole scavengers can be mainly ascribed to the difference of proton reduction potentials caused by the pH variations.[61,62] The catalytic solution switched from an acidic condition (pH = 3) when using AA as the hole scavenger to a basic condition (pH = 9) when using the other three hole scavengers (note that the QD-Au HNCs were transferred from toluene to an alkaline solution). Based on the Nernst equation, proton reduction with AA as the hole scavenger requires a much smaller driving force (0.354 V vs NHE) compared to other three catalytic systems.[63,64] The pH effect of reaction solution was further confirmed by testing the HER activity using MeOH as the hole scavenger under acidic conditions (pH = 3). Results showed that an increase of H_2 evolution of around 6-fold was achieved after changing the pH from 9 to 3 (Figure S18). However, the catalytic activity under this condition was still significantly lower than that when AA was used as the hole scavenger (pH = 3), demonstrating that other factors such as binding affinity between the hole scavengers and the HNCs may also play a role. Moreover, the benignity of AA to the QD-Au HNCs, evidenced by the nearly unchanged absorption spectral profile after the photocatalytic reaction (Figure S19), could explain the stable H_2 evolution rate over a long period of time. Control catalytic trials performed with the absence of any necessary components, i.e., AA, light irradiation, or HNC catalyst, all showed no HER activity, further confirming the nature of the HNC photocatalyzed reaction (Figure S20).

https://doi.org/10.1021/jacs.3c06065
J. Am. Chem. Soc. 2023, 145, 21886−21896

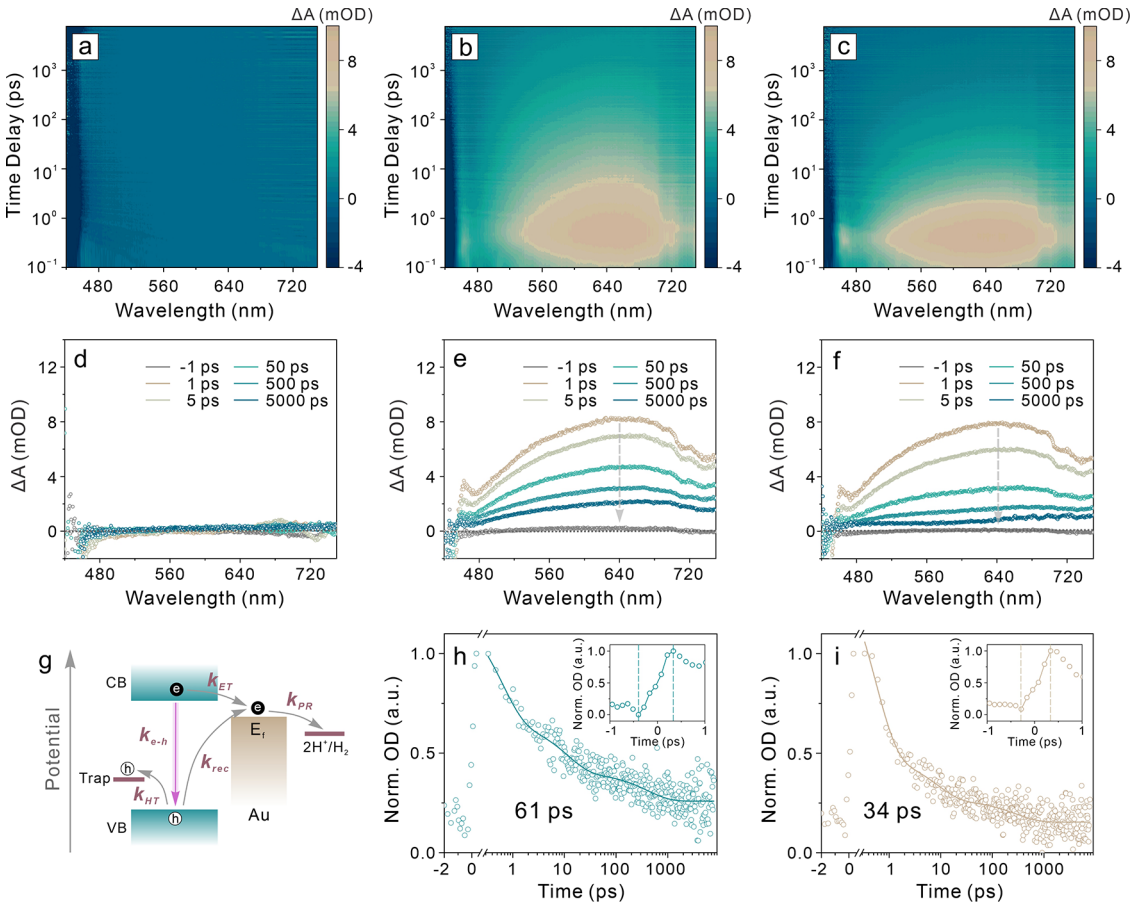

Figure 4. TA spectroscopic studies on charge carrier dynamics. (a–c) Pseudo color maps of CdS/ZnS QDs (a), QD-$Au_{1.6}$ HNCs (b), and QD-$Au_{3.3}$ HNCs (c). (d–f) ΔA spectra at different time delays of CdS/ZnS QDs (d), QD-$Au_{1.6}$ HNCs (e), and QD-$Au_{3.3}$ HNCs (f). (g) Schematic illustration of the charge transfer processes of the QD-Au HNCs in HER. (h, i) Kinetics probed at 460 nm for QD-$Au_{1.6}$ HNCs (h) and QD-$Au_{3.3}$ HNCs (i).

We then investigated the Au domain size effect on the catalytic efficiency of HER. Four samples, i.e., CdS/ZnS QDs and QD-$Au_{1.6}$, QD-$Au_{2.2}$, and QD-$Au_{3.3}$ HNC samples (Figure S21), were tested and compared (Figure 3 c, d). The average H_2 generation rates were measured to be 9.77 ± 0.37 μmol g_{cat}^{-1} h^{-1}, 2.10 ± 0.12 mmol g_{cat}^{-1} h^{-1}, 1.12 ± 0.09 mmol g_{cat}^{-1} h^{-1}, and 0.58 ± 0.06 mmol g_{cat}^{-1} h^{-1}, for core/shell CdS/ZnS QDs, QD-$Au_{1.6}$, QD-$Au_{2.2}$, and QD-$Au_{3.3}$ HNCs, respectively (Figure 3c, d). An over 200-fold enhancement was shown when comparing the HER rates of QD-$Au_{1.6}$ HNCs and bare CdS/ZnS host QDs. To eliminate the influences of different extinction coefficients and different numbers of the HNC catalysts with unit mass, we normalized the HER rate to the same mass of applied CdS/ZnS QD hosts (details were shown in SI), shown in Figure 3d. The corrected HER rates were measured to be 9.77 ± 0.37 μmol g_{QD}^{-1} h^{-1}, 4.97 ± 0.28 mmol g_{QD}^{-1} h^{-1}, 4.16 ± 0.11 mmol g_{QD}^{-1} h^{-1}, and 3.49 ± 0.38 mmol g_{QD}^{-1} h^{-1}, for QDs, QD-$Au_{1.6}$, QD-$Au_{2.2}$, and QD-$Au_{3.3}$ HNCs, respectively. A highest over 400-fold enhancement of HER rate after Au growth was then achieved after normalization. The same trend of increased HER catalytic efficiency with decreasing size of Au satellite domains in HNCs was also observed when using Na_2S + Na_2SO_3 as hole scavengers in a basic condition (pH = 9, Figure S22). The correlation between Au sizes in HNCs and their HER rates can be majorly attributed to the Au Fermi level shifting and the differences of charge carrier dynamics. Upon illumination, the electron density of the Au domains of HNCs increases due to electron transfer from QD hosts to Au satellites and the superior electron storage property of the Au domains.[65,66] As a consequence, the Au Fermi level shifts toward the conduction band (CB) edge (a more negative value) of the QD host.[67,68] The Fermi level exhibits a greater shift for the HNC system with smaller Au domains due to their quantized energy levels.[69] Therefore, decreasing the Au domain size in HNCs leads to an increased reducing power, thus an enhanced catalytic performance in HER.[69,70] Besides, the effect of photogenerated charge carrier dynamics of the QD-Au HNCs with different Au domain sizes on the HER will be discussed in the next section. We also performed the photocatalyst stability tests, and the results showed that the HNCs could go through at least three cycles of HER with almost identical H_2 evolution profiles (Figure 3e). Moreover, the catalytic profile showed nearly no change after storage of the HNC catalysts at ambient conditions for one month (Figure 3e), demonstrating its excellent stability for long-term use.

To further prove that the integrity of the CdS/ZnS QD-Au HNCs was imperative to the superior HER photocatalytic performance, a series of control groups under the same reaction conditions were evaluated for comparison (Figure 3f). Neither pure Au NCs (average diameter 2.0 ± 0.5 nm, Figure S23) nor a mixture of CdS/ZnS QDs and Au NCs (QD+Au) with a Au to QD ratio being the same as that in QD-$Au_{1.6}$ HNCs showed any HER activity (Figure 3f). In addition, when

https://doi.org/10.1021/jacs.3c06065
J. Am. Chem. Soc. 2023, 145, 21886–21896

the MUA capped CdS QDs were used as the catalysts (Figure S24), an extremely low HER rate of 1.67 ± 0.05 μmol g_{cat}^{-1} h^{-1} was obtained, which was even much lower than that of CdS/ZnS core/shell QDs (9.77 ± 0.37 μmol g_{cat}^{-1} h^{-1}, Figure 3f, inset). This can be explained by the presence of abundant low-energy surface trap states that diminish the number of available photogenerated electrons in the case of CdS core-only QD photocatalysts (Figure 3f).[23] By depositing Au satellite domains directly to CdS QDs (Figure S25), a higher catalytic efficiency (0.39 ± 0.03 mmol g_{cat}^{-1} h^{-1}) can be obtained, however, still much lower than that of the CdS/ZnS QD-Au HNCs with a similar Au domain size (Figure 3f). Together, these control experiments unambiguously demonstrated that the heterostructural integrity of the CdS/ZnS core/shell QD-Au HNCs was required and responsible for the observed high HER photocatalytic efficiencies.

2.4. Charge Carrier Dynamics of HNCs Characterized by TA Measurements. The significant catalytic efficiency enhancement of QD-Au HNCs can only be rationalized by the altered charge carrier dynamics due to the growth of the metallic Au domains on the CdS/ZnS core/shell QDs. To investigate such charge transfer dynamics, we carried out TA spectroscopic measurements for CdS/ZnS QDs, QD-$Au_{1.6}$ HNCs, and QD-$Au_{3.3}$ HNCs. The samples were excited by a femtosecond (fs) pulse laser at 400 nm with a pulse energy of 1 μJ at 500 Hz repetition rate. Figure 4a–c presented the two-dimensional pseudocolor TA spectra plots of the three samples. Only a negative signal (~440 nm) originated from the ground state exciton bleaching was observed for the pure CdS/ZnS QDs.[71] In contrast, a broad positive absorption signal at around 550–720 nm can be clearly visualized for both QD-Au HNC samples, which was assigned to the photo-induced absorption (PA) of holes.[72,73] Moreover, a clearly defined sharp positive feature at ~460 nm appeared next to the exciton bleach signal. This feature was ascribed to the charge separated state (the electrons transferred to the Au domains, leaving the holes in the QDs), which can generate a local electric field that leads to the red shift of the exciton transition due to Stark effect.[39,74] Note that hot electron generation and transfer from the Au satellite domains to the QD hosts should not be the main electron transfer pathway in our system due to the small Au domain sizes with minimal surface plasmon resonance effect.[75,76] This was also confirmed by solely exciting the Au domains of HNCs using a 520 nm laser, and no detectable catalytic activity was observed (Figure S26). Transient absorption (ΔA) spectra of QDs and QD-Au HNCs further provided quantitative demonstration of these characteristics, showing that both the PA and charge separated signals reached the maxima within 1 ps for both QD-Au HNC samples (Figure 4d–f), suggesting an ultrafast electron transfer process from QD host to Au satellite domains.[37,39]

In a simplified model describing the photocatalytic process using semiconductor–metal heterostructures (Figure 4g),[77] photogenerated electrons from the CB of the semiconductor QDs will first transfer to the metal domain (rate constant k_{ET}), which competes with the electron–hole recombination (rate constant k_{e-h}) and hole trapping (rate constant k_{HT}, independent of metal domain size[74]). The electrons transferred to the metal domain will then reduce protons (rate constant k_{PR}), which competes with the back recombination of electrons with holes in the semiconductor region (rate constant k_{rec}). Therefore, the overall catalytic efficiency can be determined by the following equation:[77]

$$QE_{H_2} = QE_{ET} \times QE_{PR} = \frac{k_{ET}}{(k_{ET} + k_{e-h} + k_{HT})} \times \frac{k_{PR}}{(k_{PR} + k_{rec})} \quad (1)$$

where QE_{H_2}, QE_{ET}, and QE_{PR} are the quantum efficiencies of H_2 evolution, electron transfer, and proton reduction, respectively. For Type-I CdS/ZnS core/shell QDs, due to the large confinement potential of the ZnS shell, the electron transfer process (considered as electron migration to the ZnS surface) happens with a low probability, leading to a low QE_{ET}. Therefore, bare CdS/ZnS QDs showed a negligible catalytic H_2 generation efficiency. The TA results revealed that Au deposition could facilitate the H_2 generation of CdS/ZnS QDs through significantly increasing the electron transfer rate, ultimately improving QE_{H_2}.

When comparing the pseudocolor plots and ΔA spectra between QD-$Au_{1.6}$ and QD-$Au_{3.3}$ HNCs, very similar charge transfer features were observed (Figure 4b, c, e, f). To thoroughly understand the differences in charge transfer dynamics between QD-$Au_{1.6}$ and QD-$Au_{3.3}$ HNCs, we compared their kinetics at 460 nm to decipher both electron transfer and charge recombination processes, as shown in Figure 4h and i. The rise of the signal at 460 nm showed that a subpicosecond charge separation occurred in both QD-$Au_{1.6}$ (Figure 4h inset) and QD-$Au_{3.3}$ HNCs (Figure 4i inset). Considering the time resolution of the instrument (~0.4 ps), the charge separation rates for both HNCs were too fast to be distinguished from the instrument response. Notably, the time scale of the electron transfer (sub-ps) was considerably faster than most semiconductor–metal systems and also semiconductor–adsorbate systems (typically in a time scale of a few ps to ns).[35,36,72,74,77−79] Meanwhile, the ΔA signal at 460 nm for both HNC samples decayed quickly with an average lifetime of <100 ps (Figure 4h, i), suggesting that the charge recombination rates in both samples were also fast. This phenomenon was different from what has been reported in semiconductor–metal nanorods, where the charge-separated states often had a much longer lifetime in a microsecond time scale.[35] However, the contrast between the time scales of the formation and decay of the charge separation aligned well with the high catalytic efficiency of the HNCs for H_2 generation. The short charge separation state can be partially attributed to the small size of QDs in our HNCs, reducing the spatial distance for charge recombination.[80] It could also be related to the quick capture of electrons (from Au domains) by surrounding water molecules and the absence of hole scavengers for TA measurements, which resulted in accumulation of holes within the QD hosts that accelerated electron–hole recombination through Coulomb interaction. Though short-lived, the decay of the ΔA signal at 460 nm clearly revealed that the QD-$Au_{3.3}$ HNCs had a shorter charge retention time of 34 ps (faster charge recombination rate after separation) than that of the QD-$Au_{1.6}$ HNCs (61 ps, Figure 4h, i, Table S7), which paralleled with the theoretical prediction modeled as a hole transfer from semiconductor to metal domains by Auger processes.[77] Moreover, we also fitted PA signal (at 600 nm) decay kinetics for both samples as an alternative means to extract charge retention time in semiconductor–metal heterostructures.[35] Consistently, slower charge recombination for QD-$Au_{1.6}$ HNCs was also observed (Table S7). Thus, we believed that the faster charge recombination rate, i.e., higher k_{rec} with increased Au domain

https://doi.org/10.1021/jacs.3c06065
J. Am. Chem. Soc. 2023, 145, 21886–21896

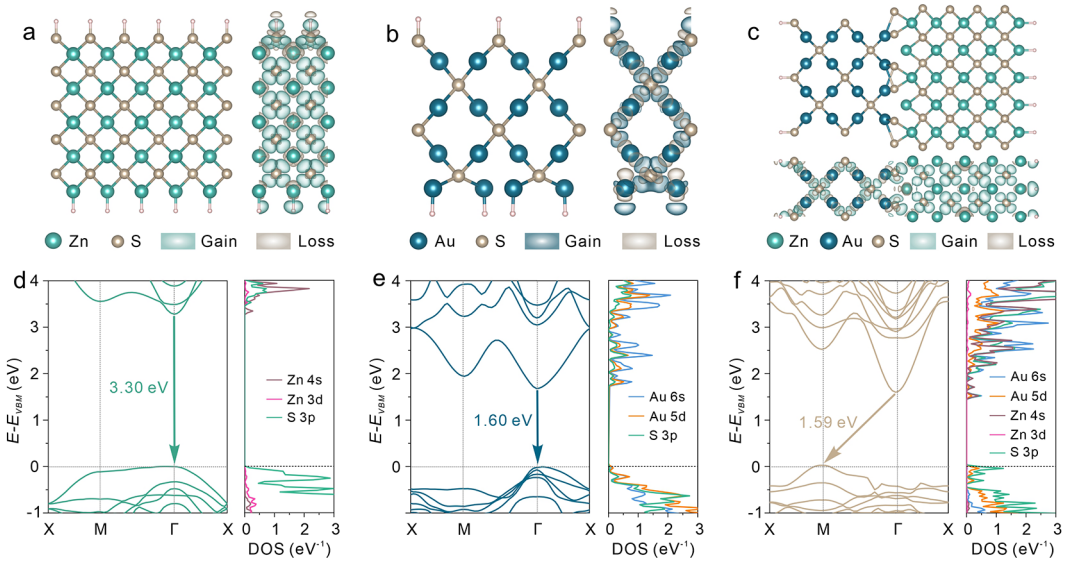

Figure 5. DFT calculations of the systems. (a–c) Atomic configurations and the corresponding charge density differences of ZnS (a), Au_2S (b), and ZnS-Au_2S (c). (d–f) Calculated band structures and the corresponding projected DOS for the three atomic configurations. The VBM was set to zero as indicated by the gray dashed lines.

size, could contribute to the decreased H_2 generation rate, as shown in the negative dependence of the catalytic efficiency on Au domain sizes (Figure 3c, d).

Besides, we proved that the QD-Au HNCs can further transfer electrons effectively to molecular electron acceptors (i.e., $ExBox^{4+}$ molecules). $ExBox^{4+}$ has previously been adopted as an electron acceptor to study electron transfer processes in CdS QD-based systems.[78] Upon accepting electrons, its reduced states, for example, $ExBox^{3+}$, exhibits spectrally distinguishable TA features from $ExBox^{4+}$.[81,82] While no electron transfer from QDs to $ExBox^{4+}$ was observed, the TA spectra for both QD-$Au_{1.6}$ and QD-$Au_{3.3}$ HNCs exhibited a positive absorption signal at ~530 nm (corresponding to $Exbox^{3+}$ and possibly $ExBox^{2+}$ generation), which reached its signal maximum within 1 ps (Figure S27). These results provided direct evidence of efficient electron transfer from the QD-Au HNCs to surrounding molecular substrates.

2.5. DFT Calculations and Photocatalytic Reaction Mechanism. Both the photocatalytic results and ultrafast TA spectroscopy measurements revealed that the photogenerated electrons and holes can be efficiently delocalized and can reach the surface of QD-Au HNCs despite the Type-I band alignment of the CdS/ZnS host QDs. To explore the underlying mechanism for such an unexpected electron delocalization phenomenon, which required the charge carriers to overcome the energy gap set by the ZnS shell, DFT calculations of the QD-Au heterojunction at the interface between the QD host and Au domain were performed to offer a thermodynamic point of view for the system.

Specifically, we calculated the charge density differences and electronic structures for three different atomic configurations, i.e., ZnS (the shell layer of the QD host), Au_2S (the interfacial layer between the QD host and Au domain), and ZnS-Au_2S (the heterojunction at the interface of QD-Au HNCs) (Figure 5a–c). Hydrogen passivation (saturate the surface bonds in the c-direction with –H groups) was applied to stabilize the structures, which has proven to show minimal effects on the calculated band structures and bandgap energies.[83,84] First, the charge density difference and Bader charge analysis revealed that an increased charge accumulation around the interfacial S atoms can be obtained for the heterojunction ZnS-Au_2S structure as compared to that for the pure ZnS and Au_2S configurations (Figure 5a–c).[85] Quantitatively, the charge donation of Au increased from $-0.13e$ to $-0.19e$, and the S atom accepted a total of around $0.54e$ from both Au and Zn atoms, doubled the charge accumulation on S atoms compared to the Au_2S ($0.26e$) system (Table S8). Such high charge loss and gain indicated a strong Au–S ionic bond formation at the interface of the HNCs, consistent with the experimental observations.

Next, the band structure calculation results showed that a direct bandgap of 3.30 eV can be obtained for ZnS with both the valence band maximum (VBM) and the conduction band minimum (CBM) located at the Γ symmetry point (Figure 5d). The projected density of states (DOS) revealed that the VBM was predominantly composed of S 3p orbitals, and the CBM comprised mainly Zn 4s and S 3p orbitals (Figure 5d). The band structure of Au_2S manifested a much narrower direct bandgap of 1.6 eV (Figure 5e), which paralleled with the bandgap energies obtained both experimentally (1.8 eV)[86] and theoretically (1.0–3.6 eV).[87] The Au 6s and 5d orbitals, and S 3p orbitals all contributed to both VBM and CBM of Au_2S (Figure 5e). The fact that Au_2S possessed a smaller bandgap than that of ZnS implied that the formation of the heterostructural interface (ZnS-Au_2S) through Au domain growth was likely to reduce the potential barrier of the ZnS shell. Indeed, a small indirect bandgap of 1.59 eV was obtained for the ZnS-Au_2S heterojunction structure, with VBM and CBM located at M and Γ symmetry points, respectively (Figure 5f). The smaller bandgap of the heterostructure than that of pure ZnS confirmed our hypothesis that the potential barrier set by the wide-bandgap ZnS shell for Type-I CdS/ZnS core/shell QDs can be lowered through the heterojunction formation between QD hosts and Au domains. The projected DOS calculation demonstrated that both the Au 5d and S 3p orbitals contributed largely to the CBM and VBM of the heterostructure (Figure 5f), further proving that the interfacial Au_2S layer played an important role in altering the band

https://doi.org/10.1021/jacs.3c06065
J. Am. Chem. Soc. 2023, 145, 21886–21896

Scheme 1. Schematic Illustration of the Photocatalytic Mechanism for the QD-Au HNCs Compared with the Type-I CdS/ZnS Core/Shell QDs Counterpart (dHA indicates dehydroascorbic acid).

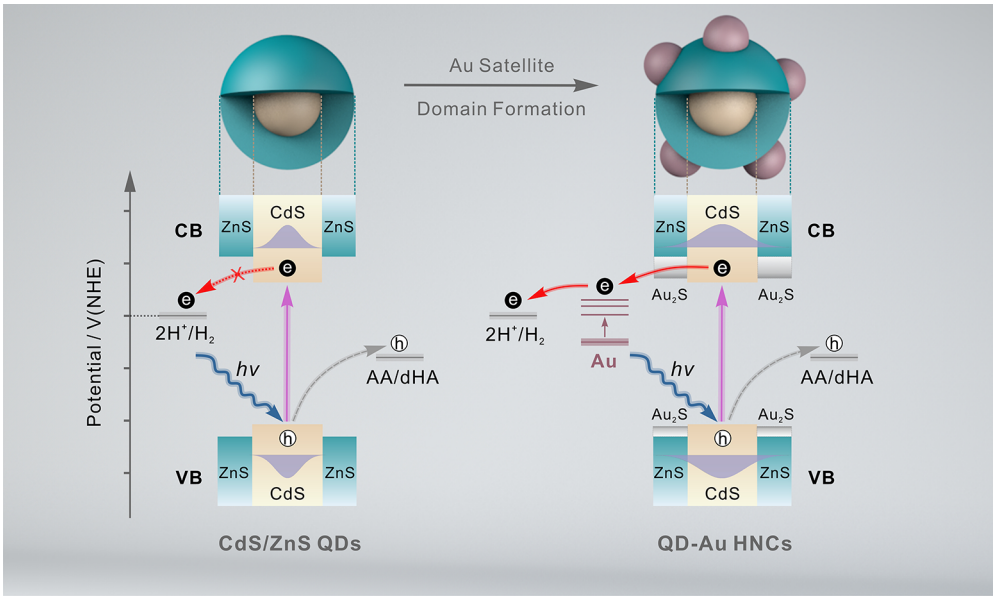

structure of the HNCs. In addition, much reduced effective masses of electrons (m_e*) and holes (m_h*) for ZnS-Au_2S were calculated compared to that of ZnS, indicating higher charge carrier mobilities through the formation of Au_2S interfacial layer (Table S9), agreed well with the photocatalytic measurements and TA results.

Taking all of the experimental data and theoretical calculation results together, the overall catalytic mechanism can be summarized in Scheme 1. First, the Type-I CdS/ZnS core/shell QDs exhibit low catalytic efficiency due to the strong quantum confinement installed by the wide-bandgap ZnS shell. Only a small population of photogenerated electrons and holes can tunnel through the potential barrier of ZnS shell and subsequently perform proton reduction and AA oxidation, respectively. The growth of metallic Au domains locally creates a ZnS-Au_2S heterojunction at the CdS/ZnS-Au interface, which facilitates the charge separation and migration to the particle surface by lowering the energy barrier (weakening the quantum confinement) of Type-I band structure and increasing the charge carrier mobility. Upon illumination, the photogenerated electrons and holes in HNCs can be rapidly separated within 1 ps and migrate to the HNC particle surface. The electrons can be efficiently captured by metallic Au domains for subsequent hydrogen generation, while the holes are consumed by the hole scavenger AA. The negative correlation between the Au satellite domain size and corresponding HER efficiency is a result of increased charge recombination rate and reduced Fermi level shifting when increasing the Au domain size of QD-Au HNCs.

3. CONCLUSION

In conclusion, we successfully synthesized a set of CdS/ZnS QD-Au host-satellite-type HNCs with different Au metallic domain sizes. A maximum of over 400 times higher HER efficiency was achieved when using the HNCs as photocatalysts, compared to the bare CdS/ZnS core/shell QDs counterpart. A negative correlation between Au domain sizes and catalytic efficiency, that is, increased efficiency with decreasing Au domain sizes, was obtained. TA studies revealed that while the electron and hole transfer in CdS/ZnS QDs were quite sluggish, ultrafast subpicosecond charge separation was observed in the QD-Au HNC systems. Kinetic studies showed that a slower charge recombination rate along with a larger Fermi level shift can be responsible for the increased H_2 generation rate for the HNC photocatalyst with smaller Au metallic domains. Based on DFT calculations, the fast charge extraction to the HNC surface was ascribed to the formation of an intermediate Au_2S layer at the QD-Au interface, lowering the energy barriers installed by the ZnS shell and liberating the confined photogenerated charges inside HNCs. Our findings not only provided a novel approach toward effective utilizations of Type-I core/shell QDs in catalysis, but also offered insights into the heterojunction effects and charge transfer kinetics of semiconductor−metal heterostructures, which will guide the future design of such hybrid materials for various applications.

■ ASSOCIATED CONTENT

Supporting Information

The Supporting Information is available free of charge at https://pubs.acs.org/doi/10.1021/jacs.3c06065.

Additional experimental and DFT calculation details, UV−vis absorption, PL, EDS, XPS, TA spectra, PL lifetime, nuclear magnetic resonance spectroscopy, thermogravimetric analysis measurements, photographs, TEM images, and catalytic results (PDF)

■ AUTHOR INFORMATION

Corresponding Author

Ou Chen − *Department of Chemistry, Brown University, Providence, Rhode Island 02912, United States;* orcid.org/0000-0003-0551-090X; Email: ouchen@brown.edu

Authors

Na Jin − *Department of Chemistry, Brown University, Providence, Rhode Island 02912, United States*

https://doi.org/10.1021/jacs.3c06065
J. Am. Chem. Soc. 2023, 145, 21886−21896

Yonglei Sun − *Institute of Materials Science, University of Connecticut, Storrs Mansfield, Connecticut 06269, United States;* orcid.org/0000-0001-6713-364X
Wenwu Shi − *School of Physical Science and Technology, Southwest University, Chongqing 400715, People's Republic of China; Institute of Information Technology, Shenzhen Institute of Information Technology, Shenzhen 518172, China*
Ping Wang − *Key Laboratory of Preparation and Applications of Environmental Friendly Materials of the Ministry of Education, College of Chemistry, Jilin Normal University, Changchun 130103, China;* orcid.org/0000-0002-7189-9418
Yasutaka Nagaoka − *Department of Chemistry, Brown University, Providence, Rhode Island 02912, United States;* orcid.org/0000-0001-8612-2612
Tong Cai − *Department of Chemistry, Brown University, Providence, Rhode Island 02912, United States*
Rongzhen Wu − *Department of Chemistry, Brown University, Providence, Rhode Island 02912, United States*
Lacie Dube − *Department of Chemistry, Brown University, Providence, Rhode Island 02912, United States*
Hawi N. Nyiera − *Department of Chemistry, University of Connecticut, Storrs Mansfield, Connecticut 06269, United States*
Yuzi Liu − *Center for Nanoscale Materials, Argonne National Laboratory, Argonne, Illinois 60439, United States;* orcid.org/0000-0002-8733-1683
Tomoyasu Mani − *Department of Chemistry, University of Connecticut, Storrs Mansfield, Connecticut 06269, United States;* orcid.org/0000-0002-4125-5195
Xinzhong Wang − *Institute of Information Technology, Shenzhen Institute of Information Technology, Shenzhen 518172, China*
Jing Zhao − *Institute of Materials Science, University of Connecticut, Storrs Mansfield, Connecticut 06269, United States; Department of Chemistry, University of Connecticut, Storrs Mansfield, Connecticut 06269, United States;* orcid.org/0000-0002-6882-2196

Complete contact information is available at: https://pubs.acs.org/10.1021/jacs.3c06065

Funding

O.C. thanks the support from the National Science Foundation under Award No. DMR-1943930 and CBET-1936223. O.C. also acknowledges the support from the Alfred P. Sloan Foundation through Sloan Research Fellowship Award program, and the 3M Foundation through the Non-Tenured Faculty Award program. J.Z. acknowledges the support from the National Science Foundation under Award No. CBET-1936228. The work performed at the Center for Nanoscale Materials, a U.S. Department of Energy Office of Science User Facility, was supported by the U.S. DOE, Office of Basic Energy Sciences, under Contract No. DE-AC02-06CH11357.

Notes

The authors declare no competing financial interest.

■ ACKNOWLEDGMENTS

O.C. acknowledges support for TEM, XRD, and XPS measurements performed at the Institute for Molecular and Nanoscale Innovation (IMNI) at Brown University. N.J. acknowledges support from SPIE Optics and Photonics Education Scholarship. Partial electron microscopy research was conducted at Argonne National Laboratory.

■ REFERENCES

(1) Cao, S.; Piao, L.; Chen, X. Emerging Photocatalysts for Hydrogen Evolution. *Trends Chem.* **2020**, *2* (1), 57−70.
(2) Tran, P. D.; Wong, L. H.; Barber, J.; Loo, J. S. C. Recent Advances in Hybrid Photocatalysts for Solar Fuel Production. *Energy Environ. Sci.* **2012**, *5* (3), 5902−5918.
(3) Wu, K.; Lian, T. Quantum Confined Colloidal Nanorod Heterostructures for Solar-to-Fuel Conversion. *Chem. Soc. Rev.* **2016**, *45* (14), 3781−3810.
(4) Mao, S. S.; Shen, S. Catalysing Artificial Photosynthesis. *Nat. Photonics* **2013**, *7* (12), 944−946.
(5) Chu, S.; Cui, Y.; Liu, N. The Path towards Sustainable Energy. *Nat. Mater.* **2017**, *16* (1), 16−22.
(6) Fujishima, A.; Honda, K. Electrochemical Photolysis of Water at a Semiconductor Electrode. *Nature* **1972**, *238* (5358), 37−38.
(7) Qi, M. Y.; Conte, M.; Anpo, M.; Tang, Z. R.; Xu, Y. J. Cooperative Coupling of Oxidative Organic Synthesis and Hydrogen Production over Semiconductor-Based Photocatalysts. *Chem. Rev.* **2021**, *121* (21), 13051−13085.
(8) Wang, Q.; Domen, K. Particulate Photocatalysts for Light-Driven Water Splitting: Mechanisms, Challenges, and Design Strategies. *Chem. Rev.* **2020**, *120* (2), 919−985.
(9) Cheng, L.; Xiang, Q.; Liao, Y.; Zhang, H. CdS-Based Photocatalysts. *Energy Environ. Sci.* **2018**, *11* (6), 1362−1391.
(10) Nasir, J. A.; Rehman, Z. u.; Shah, S. N. A.; Khan, A.; Butler, I. S.; Catlow, C. R. A. Recent Developments and Perspectives in CdS-Based Photocatalysts for Water Splitting. *J. Mater. Chem. A* **2020**, *8* (40), 20752−20780.
(11) Melnychuk, C.; Guyot-Sionnest, P. Multicarrier Dynamics in Quantum Dots. *Chem. Rev.* **2021**, *121* (4), 2325−2372.
(12) Yuan, Y.; Jin, N.; Saghy, P.; Dube, L.; Zhu, H.; Chen, O. Quantum Dot Photocatalysts for Organic Transformations. *J. Phys. Chem. Lett.* **2021**, *12* (30), 7180−7193.
(13) Kodaimati, M. S.; McClelland, K. P.; He, C.; Lian, S.; Jiang, Y.; Zhang, Z.; Weiss, E. A. Viewpoint: Challenges in Colloidal Photocatalysis and Some Strategies for Addressing Them. *Inorg. Chem.* **2018**, *57* (7), 3659−3670.
(14) Ning, X.; Li, J.; Yang, B.; Zhen, W.; Li, Z.; Tian, B.; Lu, G. Inhibition of Photocorrosion of CdS via Assembling with Thin Film TiO_2 and Removing Formed Oxygen by Artificial Gill for Visible Light Overall Water Splitting. *Appl. Catal., B* **2017**, *212*, 129−139.
(15) Ran, J.; Zhang, J.; Yu, J.; Jaroniec, M.; Qiao, S. Z. Earth-Abundant cocatalysts for Semiconductor-Based Photocatalytic Water Splitting. *Chem. Soc. Rev.* **2014**, *43* (22), 7787−7812.
(16) Veamatahau, A.; Jiang, B.; Seifert, T.; Makuta, S.; Latham, K.; Kanehara, M.; Teranishi, T.; Tachibana, Y. Origin of Surface Trap States in CdS Quantum Dots: Relationship between Size Dependent Photoluminescence and Sulfur Vacancy Trap States. *Phys. Chem. Chem. Phys.* **2015**, *17* (4), 2850−2858.
(17) Yan, Z.; Wang, W.; Du, L.; Zhu, J.; Phillips, D. L.; Xu, J. Interpreting the Enhanced Photoactivities of 0D/1D Heterojunctions of CdS Quantum Dots/TiO_2 Nanotube Arrays Using Femtosecond Transient Absorption Spectroscopy. *Appl. Catal., B* **2020**, *275*, 119151.
(18) Reiss, P.; Protiere, M.; Li, L. Core/Shell Semiconductor Nanocrystals. *Small* **2009**, *5* (2), 154−168.
(19) Greytak, A. B.; Allen, P. M.; Liu, W.; Zhao, J.; Young, E. R.; Popovic, Z.; Walker, B.; Nocera, D. G.; Bawendi, M. G. Alternating Layer Addition Approach to CdSe/CdS Core/Shell Quantum Dots with Near-Unity Quantum Yield and High On-Time Fractions. *Chem. Sci.* **2012**, *3* (6), 2028−2034.
(20) Chen, O.; Wei, H.; Maurice, A.; Bawendi, M.; Reiss, P. Pure Colors from Core-Shell Quantum Dots. *MRS Bull.* **2013**, *38* (9), 696−702.
(21) Chen, D.; Zhao, F.; Qi, H.; Rutherford, M.; Peng, X. Bright and Stable Purple/Blue Emitting CdS/ZnS Core/Shell Nanocrystals

Grown by Thermal Cycling Using a Single-Source Precursor. *Chem. Mater.* **2010**, *22* (4), 1437−1444.
(22) Selopal, G. S.; Zhao, H.; Wang, Z. M.; Rosei, F. Core/Shell Quantum Dots Solar Cells. *Adv. Funct. Mater.* **2020**, *30* (13), 1908762.
(23) Huang, L.; Wang, X.; Yang, J.; Liu, G.; Han, J.; Li, C. Dual Cocatalysts Loaded Type I CdS/ZnS Core/Shell Nanocrystals as Effective and Stable Photocatalysts for H_2 Evolution. *J. Phys. Chem. C* **2013**, *117* (22), 11584−11591.
(24) Chauviré, T.; Mouesca, J.-M.; Gasparutto, D.; Ravanat, J.-L.; Lebrun, C.; Gromova, M.; Jouneau, P.-H.; Chauvin, J.; Gambarelli, S.; Maurel, V. Redox Photocatalysis with Water-Soluble Core-Shell CdSe-ZnS Quantum Dots. *J. Phys. Chem. C* **2015**, *119* (31), 17857−17866.
(25) Huang, J.; Mulfort, K. L.; Du, P.; Chen, L. X. Photodriven Charge Separation Dynamics in CdSe/ZnS Core/Shell Quantum Dot/Cobaloxime Hybrid for Efficient Hydrogen Production. *J. Am. Chem. Soc.* **2012**, *134* (40), 16472−16475.
(26) Ben-Shahar, Y.; Banin, U. Hybrid Semiconductor-Metal Nanorods as Photocatalysts. *Top. Curr. Chem.* **2016**, *374* (4), 54.
(27) Zhu, H.; Cai, T.; Yuan, Y.; Wang, X.; Nagaoka, Y.; Zhao, J.; Liu, Z.; Li, R.; Chen, O. Pressure-Induced Transformations of Three-Component Heterostructural Nanocrystals with CdS-Au_2S Janus Nanoparticles as Hosts and Small Au Nanoparticles as Satellites. *ACS Appl. Nano Mater.* **2019**, *2* (11), 6804−6808.
(28) Zhu, H.; Fan, Z.; Yu, L.; Wilson, M. A.; Nagaoka, Y.; Eggert, D.; Cao, C.; Liu, Y.; Wei, Z.; Wang, X.; et al. Controlling Nanoparticle Orientations in the Self-Assembly of Patchy Quantum Dot-Gold Heterostructural Nanocrystals. *J. Am. Chem. Soc.* **2019**, *141* (14), 6013−6021.
(29) Zhu, H.; Fan, Z.; Yuan, Y.; Wilson, M. A.; Hills-Kimball, K.; Wei, Z.; He, J.; Li, R.; Grunwald, M.; Chen, O. Self-Assembly of Quantum Dot-Gold Heterodimer Nanocrystals with Orientational Order. *Nano Lett.* **2018**, *18* (8), 5049−5056.
(30) Zhu, H.; Nagaoka, Y.; Hills-Kimball, K.; Tan, R.; Yu, L.; Fang, Y.; Wang, K.; Li, R.; Wang, Z.; Chen, O. Pressure-Enabled Synthesis of Hetero-Dimers and Hetero-Rods through Intraparticle Coalescence and Interparticle Fusion of Quantum-Dot-Au Satellite Nanocrystals. *J. Am. Chem. Soc.* **2017**, *139* (25), 8408−8411.
(31) Wang, P.; Shi, W.; Jin, N.; Liu, Z.; Wang, Y.; Cai, T.; Hills-Kimball, K.; Yang, H.; Yang, X.; Jin, Y.; et al. Counterbalancing of Electron and Hole Transfer in Quantum Dots for Enhanced Photocatalytic H_2 Evolution. *Nano Res.* **2023**, *16* (2), 2271−2277.
(32) MacSwain, W.; Lin, H.; Li, Z.-J.; Li, S.; Chu, C.; Dube, L.; Chen, O.; Leem, G.; Zheng, W. Facilitated Electron Transfer by Mn Dopants in 1-Dimensional CdS Nanorods for Enhanced Photocatalytic Hydrogen Generation. *J. Mater. Chem. A* **2023**, *11* (13), 7066−7076.
(33) Banin, U.; Ben-Shahar, Y.; Vinokurov, K. Hybrid Semiconductor-Metal Nanoparticles: From Architecture to Function. *Chem. Mater.* **2014**, *26* (1), 97−110.
(34) Ben-Shahar, Y.; Stone, D.; Banin, U. Rich Landscape of Colloidal Semiconductor-Metal Hybrid Nanostructures: Synthesis, Synergetic Characteristics, and Emerging Applications. *Chem. Rev.* **2023**, *123* (7), 3790−3851.
(35) Wu, K.; Zhu, H.; Liu, Z.; Rodriguez-Cordoba, W.; Lian, T. Ultrafast Charge Separation and Long-Lived Charge Separated State in Photocatalytic CdS-Pt Nanorod Heterostructures. *J. Am. Chem. Soc.* **2012**, *134* (25), 10337−10340.
(36) Camargo, F. V. A.; Ben-Shahar, Y.; Nagahara, T.; Panfil, Y. E.; Russo, M.; Banin, U.; Cerullo, G. Visualizing Ultrafast Electron Transfer Processes in Semiconductor-Metal Hybrid Nanoparticles: Toward Excitonic-Plasmonic Light Harvesting. *Nano Lett.* **2021**, *21* (3), 1461−1468.
(37) Wu, K.; Chen, Z.; Lv, H.; Zhu, H.; Hill, C. L.; Lian, T. Hole Removal Rate Limits Photodriven H_2 Generation Efficiency in CdS-Pt and CdSe/CdS-Pt Semiconductor Nanorod-Metal Tip Heterostructures. *J. Am. Chem. Soc.* **2014**, *136* (21), 7708−7716.
(38) Wu, K.; Chen, J.; McBride, J. R.; Lian, T. Efficient Hot-Electron Transfer by a Plasmon-Induced Interfacial Charge-Transfer Transition. *Science* **2015**, *349* (6248), 632−635.
(39) Wu, K.; Rodriguez-Cordoba, W. E.; Yang, Y.; Lian, T. Plasmon-Induced Hot Electron Transfer from the Au Tip to CdS Rod in CdS-Au Nanoheterostructures. *Nano Lett.* **2013**, *13* (11), 5255−5263.
(40) Liu, Y.; Chen, Q.; Cullen, D. A.; Xie, Z.; Lian, T. Efficient Hot Electron Transfer from Small Au Nanoparticles. *Nano Lett.* **2020**, *20* (6), 4322−4329.
(41) Rasamani, K. D.; Sun, Y. Promoting Reactivity of Photoexcited Hot Electrons in Small-Sized Plasmonic Metal Nanoparticles that are Supported on Dielectric Nanospheres. *J. Chem. Phys.* **2020**, *152* (8), 084706.
(42) Zhu, H.; Fan, Z.; Song, S.; Eggert, D.; Liu, Y.; Shi, W.; Yuan, Y.; Kim, K. S.; Grunwald, M.; Chen, O. Dual Atomic Coherence in the Self-Assembly of Patchy Heterostructural Nanocrystals. *ACS Nano* **2022**, *16* (9), 15053−15062.
(43) Cao, Y. C.; Wang, J. One-Pot Synthesis of High-Quality Zinc-Blende CdS Nanocrystals. *J. Am. Chem. Soc.* **2004**, *126* (44), 14336−14337.
(44) Chen, O.; Shelby, D. E.; Yang, Y.; Zhuang, J.; Wang, T.; Niu, C.; Omenetto, N.; Cao, Y. C. Excitation-Intensity-Dependent Color-Tunable Dual Emissions from Manganese-Doped CdS/ZnS Core/Shell Nanocrystals. *Angew. Chem., Int. Ed.* **2010**, *49* (52), 10132−10135.
(45) Li, J. J.; Wang, Y. A.; Guo, W.; Keay, J. C.; Mishima, T. D.; Johnson, M. B.; Peng, X. Large-Scale Synthesis of Nearly Monodisperse CdSe/CdS Core/Shell Nanocrystals Using Air-Stable Reagents via Successive Ion Layer Adsorption and Reaction. *J. Am. Chem. Soc.* **2003**, *125* (41), 12567−12575.
(46) Yang, Y.; Chen, O.; Angerhofer, A.; Cao, Y. C. On Doping CdS/ZnS Core/Shell Nanocrystals with Mn. *J. Am. Chem. Soc.* **2008**, *130* (46), 15649−15661.
(47) Gray, V.; Xia, P.; Huang, Z.; Moses, E.; Fast, A.; Fishman, D. A.; Vullev, V. I.; Abrahamsson, M.; Moth-Poulsen, K.; Lee Tang, M. CdS/ZnS Core-Shell Nanocrystal Photosensitizers for Visible to UV Upconversion. *Chem. Sci.* **2017**, *8* (8), 5488−5496.
(48) Mokari, T.; Rothenberg, E.; Popov, I.; Costi, R.; Banin, U. Selective Growth of Metal Tips onto Semiconductor Quantum Rods and Tetrapods. *Science* **2004**, *304* (5678), 1787−1790.
(49) Hostetler, M. J.; Wingate, J. E.; Zhong, C.-J.; Harris, J. E.; Vachet, R. W.; Clark, M. R.; Londono, J. D.; Green, S. J.; Stokes, J. J.; Wignall, G. D.; et al. Alkanethiolate Gold Cluster Molecules with Core Diameters from 1.5 to 5.2 nm: Core and Monolayer Properties as a Function of Core Size. *Langmuir* **1998**, *14* (1), 17−30.
(50) Amendola, V.; Pilot, R.; Frasconi, M.; Marago, O. M.; Iati, M. A. Surface Plasmon Resonance in Gold Nanoparticles: a Review. *J. Condens. Matter Phys.* **2017**, *29* (20), 203002.
(51) Costi, R.; Saunders, A. E.; Banin, U. Colloidal Hybrid Nanostructures: a New Type of Functional Materials. *Angew. Chem., Int. Ed.* **2010**, *49* (29), 4878−4897.
(52) Pramanik, G.; Humpolickova, J.; Valenta, J.; Kundu, P.; Bals, S.; Bour, P.; Dracinsky, M.; Cigler, P. Gold Nanoclusters with Bright Near-Infrared Photoluminescence. *Nanoscale* **2018**, *10* (8), 3792−3798.
(53) Cheng, Y.; Lu, S.; Xu, W.; Wen, H.; Wang, J. Fabrication of Superhydrophobic Au-Zn Alloy Surface on a Zinc Substrate for Roll-down, Self-Cleaning and Anti-Corrosion Properties. *J. Mater. Chem. A* **2015**, *3* (32), 16774−16784.
(54) Ruzicka, J.-Y.; Abu Bakar, F.; Hoeck, C.; Adnan, R.; McNicoll, C.; Kemmitt, T.; Cowie, B. C.; Metha, G. F.; Andersson, G. G.; Golovko, V. B. Toward Control of Gold Cluster Aggregation on TiO_2 via Surface Treatments. *J. Phys. Chem. C* **2015**, *119* (43), 24465−24474.
(55) van Huis, M. A.; Figuerola, A.; Fang, C.; Beche, A.; Zandbergen, H. W.; Manna, L. Chemical Transformation of Au-Tipped CdS Nanorods into AuS/Cd Core/Shell Particles by Electron Beam Irradiation. *Nano Lett.* **2011**, *11* (11), 4555−4561.

https://doi.org/10.1021/jacs.3c06065
J. Am. Chem. Soc. 2023, 145, 21886−21896

(56) Galian, R. E.; Diaz, P.; Ribera, A.; Rincón-Bertolín, A.; Agouram, S.; Pérez-Prieto, J. Controlled Building of CdSe@ZnS/Au and CdSe@ZnS/Au_2S/Au Nanohybrids. *Nano Res.* **2015**, *8* (7), 2271−2287.
(57) Fleury, B.; Cortes-Huerto, R.; Tache, O.; Testard, F.; Menguy, N.; Spalla, O. Gold Nanoparticle Internal Structure and Symmetry Probed by Unified Small-Angle X-ray Scattering and X-ray Diffraction Coupled with Molecular Dynamics Analysis. *Nano Lett.* **2015**, *15* (9), 6088−6094.
(58) Zhu, W.; Michalsky, R.; Metin, O.; Lv, H.; Guo, S.; Wright, C. J.; Sun, X.; Peterson, A. A.; Sun, S. Monodisperse Au Nanoparticles for Selective Electrocatalytic Reduction of CO_2 to CO. *J. Am. Chem. Soc.* **2013**, *135* (45), 16833−16836.
(59) Heiba, Z. K.; Mohamed, M. B.; Badawi, A. Structure, Optical and Electronic Characteristics of Iron-Doped Cadmium Sulfide under Nonambient Atmosphere. *Appl. Phys. A: Mater. Sci. Process.* **2021**, *127* (3), 166.
(60) Owen, E. A.; Yates, E. L. XLI. Precision Measurements of Crystal Parameters. *Lond. Edinb. Dublin Philos. Mag. J. Sci.* **1933**, *15* (98), 472−488.
(61) Kosco, J.; Gonzalez-Carrero, S.; Howells, C. T.; Fei, T.; Dong, Y.; Sougrat, R.; Harrison, G. T.; Firdaus, Y.; Sheelamanthula, R.; Purushothaman, B.; et al. Generation of Long-Lived Charges in Organic Semiconductor Heterojunction Nanoparticles for Efficient Photocatalytic Hydrogen Evolution. *Nat. Energy* **2022**, *7* (4), 340−351.
(62) Zong, X.; Miao, X.; Hua, S.; An, L.; Gao, X.; Jiang, W.; Qu, D.; Zhou, Z.; Liu, X.; Sun, Z. Structure Defects Assisted Photocatalytic H_2 Production for Polythiophene Nanofibers. *Appl. Catal., B* **2017**, *211*, 98−105.
(63) Huang, W.-Y.; Shen, Z.-Q.; Cheng, J.-Z.; Liu, L.-L.; Yang, K.; Chen, X.; Wen, H.-R.; Liu, S. Y. C-H Activation Derived CPPs for Photocatalytic Hydrogen Production Excellently Accelerated by a DMF Cosolvent. *J. Mater. Chem. A* **2019**, *7* (42), 24222−24230.
(64) Hu, Z.; Zhang, X.; Yin, Q.; Liu, X.; Jiang, X.-f.; Chen, Z.; Yang, X.; Huang, F.; Cao, Y. Highly Efficient Photocatalytic Hydrogen Evolution from Water-Soluble Conjugated Polyelectrolytes. *Nano Energy* **2019**, *60*, 775−783.
(65) Chen, S.; Ingram, R. S.; Hostetler, M. J.; Pietron, J. J.; Murray, R. W.; Schaaff, T. G.; Khoury, J. T.; Alvarez, M. M.; Whetten, R. L. Gold Nanoelectrodes of Varied Size: Transition to Molecule-Like Charging. *Science* **1998**, *280* (5372), 2098−2101.
(66) Kamat, P. V. Photophysical, Photochemical and Photocatalytic Aspects of Metal Nanoparticles. *J. Phys. Chem. B* **2002**, *106* (32), 7729−7744.
(67) Wood, A.; Giersig, M.; Mulvaney, P. Fermi Level Equilibration in Quantum Dot-Metal Nanojunctions. *J. Phys. Chem. B* **2001**, *105* (37), 8810−8815.
(68) Subramanian, V.; Wolf, E. E.; Kamat, P. V. Green Emission to Probe Photoinduced Charging Events in ZnO-Au Nanoparticles. Charge Distribution and Fermi-Level Equilibration. *J. Phys. Chem. B* **2003**, *107* (30), 7479−7485.
(69) Subramanian, V.; Wolf, E. E.; Kamat, P. V. Catalysis with TiO_2/Gold Nanocomposites. Effect of Metal Particle Size on the Fermi Level Equilibration. *J. Am. Chem. Soc.* **2004**, *126* (15), 4943−4950.
(70) Hendon, C. H.; Hunt, S. T.; Milina, M.; Butler, K. T.; Walsh, A.; Roman-Leshkov, Y. Realistic Surface Descriptions of Heterometallic Interfaces: The Case of TiWC Coated in Noble Metals. *J. Phys. Chem. Lett.* **2016**, *7* (22), 4475−4482.
(71) Das, S.; Rakshit, S.; Datta, A. Interplay of Multiexciton Relaxation and Carrier Trapping in Photoluminescent CdS Quantum Dots Prepared in Aqueous Medium. *J. Phys. Chem. C* **2020**, *124* (51), 28313−28322.
(72) Huang, J.; Huang, Z.; Jin, S.; Lian, T. Exciton Dissociation in CdSe Quantum Dots by Hole Transfer to Phenothiazine. *J. Phys. Chem. C* **2008**, *112* (49), 19734−19738.
(73) Tyagi, P.; Kambhampati, P. False Multiple Exciton Recombination and Multiple Exciton Generation Signals in Semiconductor Quantum Dots Arise from Surface Charge Trapping. *J. Chem. Phys.* **2011**, *134* (9), 094706.
(74) Liu, Y.; Yang, W.; Chen, Q.; Cullen, D. A.; Xie, Z.; Lian, T. Pt Particle Size Affects Both the Charge Separation and Water Reduction Efficiencies of CdS-Pt Nanorod Photocatalysts for Light Driven H_2 Generation. *J. Am. Chem. Soc.* **2022**, *144* (6), 2705−2715.
(75) Link, S.; El-Sayed, M. A. Size and Temperature Dependence of the Plasmon Absorption of Colloidal Gold Nanoparticles. *J. Phys. Chem. B* **1999**, *103* (21), 4212−4217.
(76) Huang, X.; El-Sayed, M. A. Gold Nanoparticles: Optical Properties and Implementations in Cancer Diagnosis and Photothermal Therapy. *J. Adv. Res.* **2010**, *1* (1), 13−28.
(77) Ben-Shahar, Y.; Scotognella, F.; Kriegel, I.; Moretti, L.; Cerullo, G.; Rabani, E.; Banin, U. Optimal Metal Domain Size for Photocatalysis with Hybrid Semiconductor-Metal Nanorods. *Nat. Commun.* **2016**, *7*, 10413.
(78) Young, R. M.; Jensen, S. C.; Edme, K.; Wu, Y.; Krzyaniak, M. D.; Vermeulen, N. A.; Dale, E. J.; Stoddart, J. F.; Weiss, E. A.; Wasielewski, M. R.; et al. Ultrafast Two-Electron Transfer in a CdS Quantum Dot-Extended-Viologen Cyclophane Complex. *J. Am. Chem. Soc.* **2016**, *138* (19), 6163−6170.
(79) Mongin, D.; Shaviv, E.; Maioli, P.; Crut, A.; Banin, U.; Del Fatti, N.; Vallée, F. Ultrafast Photoinduced Charge Separation in Metal-Semiconductor Nanohybrids. *ACS Nano* **2012**, *6* (8), 7034−7043.
(80) Xin, Z. K.; Gao, Y. J.; Gao, Y.; Song, H. W.; Zhao, J.; Fan, F.; Xia, A. D.; Li, X. B.; Tung, C. H.; Wu, L. Z. Rational Design of Dot-on-Rod Nano-Heterostructure for Photocatalytic CO_2 Reduction: Pivotal Role of Hole Transfer and Utilization. *Adv. Mater.* **2022**, *34* (3), No. e2106662.
(81) Dyar, S. M.; Barnes, J. C.; Juricek, M.; Stoddart, J. F.; Co, D. T.; Young, R. M.; Wasielewski, M. R. Electron Transfer and Multi-Electron Accumulation in $ExBox^{4+}$. *Angew. Chem., Int. Ed.* **2014**, *53* (21), 5371−5375.
(82) Young, R. M.; Dyar, S. M.; Barnes, J. C.; Juricek, M.; Stoddart, J. F.; Co, D. T.; Wasielewski, M. R. Ultrafast Conformational Dynamics of Electron Transfer in $ExBox^{4+}$ Subsetperylene. *J. Phys. Chem. A* **2013**, *117* (47), 12438−12448.
(83) Cojocaru, O.; Lepadatu, A. M.; Nemnes, G. A.; Stoica, T.; Ciurea, M. L. Bandgap Atomistic Calculations on Hydrogen-Passivated GeSi Nanocrystals. *Sci. Rep.* **2021**, *11* (1), 13582.
(84) Nolan, M.; O'Callaghan, S.; Fagas, G.; Greer, J. C.; Frauenheim, T. Silicon Nanowire Band Gap Modification. *Nano Lett.* **2007**, *7* (1), 34−38.
(85) Henkelman, G.; Arnaldsson, A.; Jónsson, H. A Fast and Robust Algorithm for Bader Decomposition of Charge Density. *Comput. Mater. Sci.* **2006**, *36* (3), 354−360.
(86) Suárez, J. A.; Plata, J. J.; Márquez, A. M.; Sanz, J. F. Structural, Electronic and Optical Properties of Copper, Silver and Gold Sulfide: a DFT Study. *Theor. Chem. Acc.* **2016**, *135* (3), 70.
(87) Wu, Q.; Xu, W. W.; Lin, D.; Wang, J.; Zeng, X. C. Two-Dimensional Gold Sulfide Monolayers with Direct Band Gap and Ultrahigh Electron Mobility. *J. Phys. Chem. Lett.* **2019**, *10* (13), 3773−3778.

https://doi.org/10.1021/jacs.3c06065
J. Am. Chem. Soc. 2023, 145, 21886−21896